

JWST-DECO: Temporal Variations in the Mid-IR Silicate Features of Two T Tauri Discs Based on Spitzer and JWST observations

N. Sameshima,^{1,2*} T. Miyata,³ T. Kamizuka,³ Y. Aikawa,¹ M. Honda,⁴ L. I. Cleeves,⁵ N. P. Ballering,^{6,7} M. J. Colmenares,⁸ C. González-Ruilova,^{9,10,11} V. V. Guzman,^{10,12} T. J. Haworth,¹³ C. J. Law^{5,14} and J. P. Williams¹⁵

¹Department of Astronomy, Graduate School of Science, The University of Tokyo, 7-3-1 Hongo, Bunkyo-ku, Tokyo 113-0033, Japan

²Japan Aerospace Exploration Agency, Institute of Space and Astronautical Science, 3-1-1 Yoshinodai, Chuo-ku, Sagami-hara-shi, Kanagawa 252-5210, Japan

³Institute of Astronomy, Graduate School of Science, The University of Tokyo, Osawa 2-21-1, Mitaka, Tokyo 181-0015, Japan

⁴Department of Biosphere-Geosphere Science, Okayama University of Science, 1-1 Ridai-cho, Kita-ku, Okayama 700-0005, Japan

⁵Department of Astronomy, University of Virginia, Charlottesville, VA 22904, USA

⁶Space Science Institute, Boulder, CO 80301, USA

⁷Department of Astronomy, University of Wisconsin-Madison, Madison, WI 53706, USA

⁸Department of Astronomy, University of Michigan, Ann Arbor, MI 48109, USA

⁹Departamento de Física, Universidad de Santiago de Chile, Av. Victor Jara 3659, Santiago, Chile

¹⁰Millennium Nucleus on Young Exoplanets and their Moons (YEMS), Av. Victor Jara 3659, Santiago, Chile

¹¹Center for Interdisciplinary Research in Astrophysics and Space Exploration (CIRAS), Universidad de Santiago de Chile, Av. Victor Jara 3659, Santiago, Chile

¹²Instituto de Astrofísica, Pontificia Universidad Católica de Chile, Av. Vicuña Mackenna 4860, 7820436 Macul, Santiago, Chile

¹³Astronomy Unit, Department of Physics and Astronomy, Queen Mary University of London, Mile End Road, London E1 4NS, UK

¹⁴NASA Hubble Fellowship Program Sagan Fellow

¹⁵Institute for Astronomy, University of Hawaii, Honolulu, HI 96822, USA

Accepted XXX. Received YYY; in original form ZZZ

ABSTRACT

Mid-infrared spectra of planet-forming discs commonly show prominent silicate emission, whose spectral shape is sensitive to the disc temperature distribution as well as its mineralogical composition. We report new James Webb Space Telescope (JWST) observations of the discs around Sz 96 and IP Tau and find that their silicate emission significantly changes in the 20 years since they were observed with the Spitzer Space Telescope (SST). Significant differences between the SST and JWST spectra are found for both sources, with flux variations of 10–15% in Sz 96 and 30–35% in IP Tau. Sz 96 dimmed at $\leq 18 \mu\text{m}$ and did not change significantly at longer wavelengths, whereas IP Tau became brighter across the entire wavelength range, with a particularly strong enhancement around $10 \mu\text{m}$ in the JWST data compared to the SST data. We propose that this large degree of variability is explained by structural changes in the inner regions of the discs. Specifically, we also find that crystalline silicates exhibit lower temperatures than amorphous silicates in the JWST data of both sources. This result supports the idea that crystalline grains, formed through high-temperature annealing in the inner disc regions, have been transported outward, leading to their presence in cooler regions of the disc. While similar behavior had been reported in previous SST-based studies, the much higher spectral resolution of JWST enables clearer identification of the crystalline features.

Key words: techniques: spectroscopic < Astronomical instrumentation, methods, and techniques, methods: data analysis < Astronomical instrumentation, methods, and techniques, instrumentation: spectrographs < Astronomical instrumentation, methods, and techniques, infrared: stars < Resolved and unresolved sources as a function of wavelength, stars: variables: T Tauri, Herbig Ae/Be < Stars

1 INTRODUCTION

T Tauri stars host discs, which are the sites of planet formation. By studying their structure, dust composition, and dynamics, we can gain insights into the process of planet formation and disc evolution (Williams & Cieza 2011).

The disc is heated by radiation from the central star and emits

over a wide range of wavelengths. Recent ALMA observations at 1.3 mm trace cold dust located at distances of a few to several hundred au, revealing various substructures such as rings and cavities (Orcajo et al. 2025). Near- and mid-infrared emission originates from warmer regions located at distances of approximately 0.1 to a few au (Dullemond & Monnier 2010). According to the infrared excess relative to a stellar photosphere, the discs are classified into three categories (Espaillat et al. 2014): (1) full disc, where the infrared excess consists of dust emission with a range of temperatures, sug-

* E-mail: naotosame7010@g.ecc.u-tokyo.ac.jp

gesting that the disc is continuous from the inner region to the outer region; (2) pre-transitional disc, which has a gap separating the inner and outer discs; (3) transitional disc, which has a central hole, i.e. an almost complete absence of dust emission in the inner region of the disc.

Regarding the dust composition, silicates are the main components, and their mid-infrared emission bands arise from the hot surface layers of the discs. In addition to the characteristic amorphous silicate features around $10\ \mu\text{m}$, crystalline silicate features have also been detected (Honda et al. 2003; van Boekel et al. 2005; Kessler-Silacci et al. 2006; Watson et al. 2008). However, in the interstellar medium, silicate dust is predominantly observed in an amorphous state (Kemper et al. 2004). This suggests that some degree of silicate crystallisation processes must be taking place in protoplanetary discs.

While the exact crystallisation mechanism remains a topic of debate, one of the leading hypotheses is thermal annealing in the high-temperature inner disc region, typically at $\sim 1000\ \text{K}$ and $\sim 0.1\ \text{au}$ (Bockelée-Morvan et al. 2002). However, there have been reports of crystalline features even in the outer regions of the discs, located at a few au from the star, where the temperature is too low for annealing (Watson et al. 2008). Olofsson et al. (2009) reported that around T Tauri stars, crystalline features are detected about 3.5 times more frequently in the colder outer regions than in the warmer inner regions. Olofsson et al. (2010) pointed out that the higher detection rate of crystalline features in the colder component does not necessarily mean their higher abundance in the outer region. It could instead result from a contrast problem, where the strong $10\ \mu\text{m}$ feature of amorphous silicates in the warmer inner disc masks the weaker crystalline features. To resolve this contrast problem and reliably determine the distribution of crystalline silicates, we need higher resolution data with high signal-to-noise ratio, which is now available thanks to the James Webb Space Telescope (JWST; Rigby et al. 2023).

In addition to the dust composition, temporal variability of the spectra provides key insights into disc evolution. Young stellar objects (YSOs), including T Tauri stars, exhibit variability on time scales of days to years in both optical and infrared wavelengths (Shappee et al. 2014; Bellm 2014; Morales-Calderón et al. 2011; Stauffer et al. 2014; Wright et al. 2010; Mainzer et al. 2011). These observations have revealed the diverse nature of YSO variability. Various mechanisms contribute to the optical variability, including long-term increases in brightness due to disc instabilities (Hartmann & Kenyon 1996), short-term brightness enhancements caused by magnetically induced instabilities (Alencar et al. 2010), and periodic variations tracing the rotation of magnetic spots on the stellar surface (Grankin et al. 2008). Mid-infrared spectral variation can provide information about the dust composition and temperature distribution of discs. The spectra obtained by the Infrared Spectrograph (IRS; Houck et al. 2004) onboard the Spitzer Space Telescope (SST; Werner et al. 2004) have been especially useful. Espaillat et al. (2011) examined the SST IRS spectra of pre-transitional discs taken between 2005 and 2008 to find temporal variations, which can be explained by 10–20% change of the inner disc scale height. Temporal variability of a disc spectrum over ~ 20 years can now be investigated using SST and JWST data. This offers insights into dynamical changes occurring within, at most, the inner few au, although the observed variability is more likely to trace regions much closer to the inner rim. Jang et al. (2024b) investigated spectral variations in the T Tauri star PDS 70 by comparing the SST IRS data and the JWST Mid-Infrared Instrument Medium Resolution Spectroscopy (MIRI MRS; Argyriou et al. 2023) data, revealing changes in temperature distribution and dust composition. However, the number of studies comparing the SST and JWST spectral data

remains limited. It is important to increase the sample to understand the evolution of physical structure and dust composition in discs, as the current sample size is too small to draw statistically meaningful conclusions.

In this study, we investigate the variability of two T Tauri stars that have been observed with both the SST and the JWST. By performing model fitting of the mid-infrared spectral data, we quantitatively evaluate the changes in the disc’s temperature structure and dust composition. In addition, the JWST data have higher spectral resolution and signal-to-noise ratio than the SST data. This enables clearer identification of silicate features and provides important clues about the distribution of crystalline dust, which was previously unclear. In Section 2, we describe the observations and data processing, while Section 3 outlines the model fitting methodology. The results are presented in Section 4, followed by a discussion in Section 5, and conclusions in Section 6.

2 OBSERVATIONS AND DATA

2.1 Targets

For this study, we selected two T Tauri stars, Sz 96 and IP Tau, as our targets. They are among 80 targets of the Disc-Exoplanet C/Onnection (DECO) ALMA Large Program (PI: Ilse Cleeves; 2022.1.00875.L) to investigate the gas composition in a large sample of protoplanetary discs. The JWST spectra were taken in its follow-up programme, JWST-DECO (Proposal ID: 3228; PI: Ilse Cleeves). We selected Sz 96 and IP Tau based on three criteria: the availability of SST spectroscopic data over a wide wavelength range, the absence of nearby bright objects, and the presence of strong $10\ \mu\text{m}$ silicate features. The basic properties of these stars are summarised in Table 1. Their stellar properties are similar, but their disc structures are different, as described in the following.

Sz 96: Bredall et al. (2020) investigated the colour index of dipper stars in the Lupus star-forming region using 2MASS K_s band, WISE W3 ($12\ \mu\text{m}$) and W4 ($22\ \mu\text{m}$) bands and showed that the observed infrared excess of this object is consistent with that of a full disc. In the millimetre wavelength range observed by ALMA, Guerra-Alvarado et al. (2025) showed the dust mass of $0.5\ M_{\oplus}$ and identified a ring with a radius of about 6 au, which corresponds to a colder outer region than discussed by Bredall et al. (2020). Since inner warm dust with a mass comparable to that of the outer ring would produce detectable millimetre emission, the observation indicates that the mass of warm, mid-infrared-emitting dust in the inner disc is much smaller than that in the outer ring. Xin et al. (2023) independently estimated the disc radius to be 41 au and the dust mass to be $0.74\ M_{\oplus}$. Olofsson et al. (2010) modelled the SST IRS spectrum of Sz 96 using a combination of five dust components – olivine, pyroxene, and silica for the amorphous phase, and forsterite and enstatite for the crystalline phase – with a warm component at 230 K and a cold component at 90 K. Bredall et al. (2020) detected variability in the V band based on photometric observations by ASAS-SN from 2016 to 2019 and classified this star as a quasi-periodic dipper. Park et al. (2021) reported that Sz 96 showed variability of up to 0.35 mag in the WISE W2 band ($4.6\ \mu\text{m}$) over a 6.5-year period since 2013, indicating that this object is intrinsically variable in the mid-infrared.

IP Tau: Based on an analysis of the spectral index and the equivalent width of the $10\ \mu\text{m}$ silicate feature, Furlan et al. (2009) classified the disc of IP Tau as a pre-transitional disc. Espaillat et al. (2011) modelled the SST IRS data for IP Tau, proposing an inner and outer disc structure separated by a gap lacking optically thick material,

Table 1. Stellar properties of the targets.

Property	Sz 96	IP Tau
Spectral type	M1±0.5	K7
T_{eff} (K)	3705±171	3770±150
Distance (pc)	156±4	129
Inclination (deg)	–	45
Stellar Radius (R_{\odot})	2.0±0.5	1.3
Stellar Mass (M_{\odot})	0.5±0.1	0.51
Disc type	Full	Pre-Transitional

References: For Sz 96, the spectral type, distance, radius and mass are from [Xin et al. \(2023\)](#), and the effective temperature is from [Alcalá et al. \(2017\)](#), while the inclination is not available. For IP Tau, the inclination is from [Long et al. \(2018\)](#) and the other properties are from [Gangi et al. \(2022\)](#), with uncertainties available only for the effective temperature.

with inner-edge temperatures of 1400 and 230 K, respectively. A high-resolution observation by ALMA revealed a ring-like structure with a 10 au-wide ring at a radius of 27 au ([Long et al. 2018](#)), which is much farther out than the structures traced by mid-infrared observations. According to [Park et al. \(2021\)](#), IP Tau exhibited variability of up to 0.37 mag in the W2 band during NEOWISE photometric monitoring over a 6.5-year period starting in 2013. IP Tau was observed multiple times by SST, and a variation in the continuum slope was detected. The variation was explained by a change in the height of the inner wall by [Espaillat et al. \(2011\)](#).

2.2 SST IRS

Sz 96 was observed with the SST IRS on 15 March 2006 (programme ID: 179; PI: N. Evans), and IP Tau was observed on 8 October 2008 (programme ID: 50403; PI: N. Calvet). Both observations were carried out using the Short-Low (SL) and Long-Low (LL) modules of the IRS, covering a wavelength range of 5.2–38 μm with a spectral resolution of $R = 60\text{--}130$ ($\Delta\nu = 2300\text{--}5000 \text{ km s}^{-1}$).

The spectroscopic data used in this study were taken from the IRS Enhanced Spectrophotometric Catalogue available on the Spitzer Heritage Archive¹ (SHA; [Wu et al. 2010](#)). In the reduction process of the data, the one-dimensional spectra were taken from the background-subtracted Post-BCD ("bksub.tbl") products. For each nod position, the median spectrum was computed from all exposures, and the two nod spectra were then averaged to produce the final spectrum. The flux uncertainty for each nod spectrum was derived from the "bkunc.fits" file, and the final uncertainty was computed by adding the two in quadrature ([IRS Instrument Team & Science User Support Team 2021](#)).

We compared the spectra with those obtained from the Cornell Atlas of Spitzer/IRS Sources (CASSIS²; [Lebouteiller et al. 2015](#)), which provides publishable-quality, flux-calibrated IRS spectra, and found that the fluxes between the two datasets are consistent within the uncertainties. The weighted mean of $(F_{\text{CAS}}/F_{\text{SHA}} - 1)$ is $2.87 \pm 0.17\%$ for Sz 96 and $2.41 \pm 0.41\%$ for IP Tau, indicating that the CASSIS spectra are slightly brighter than those from SHA. However, the differences are small ($\leq 3\%$) within the expected calibration uncertainties, and are not expected to substantially alter our interpretation of the observed variability.

¹ <https://irsa.ipac.caltech.edu/applications/Spitzer/SHA/>

² <https://cassis.sirtf.com/>

2.3 JWST MIRI MRS

Sz 96 and IP Tau were observed with JWST MIRI MRS on 28 July 2024, as part of the GO Cycle 2 JWST-DECO programme. The wavelength range covered by the MRS mode is 4.9–27.9 μm , with a spectral resolution of $R = 1500\text{--}3500$ ($\Delta\nu = 100\text{--}200 \text{ km s}^{-1}$).

The spectral data were processed using the JWST Calibration Pipeline v1.18.0 ([Bushouse et al. 2025](#)) and further reduced with the JDISCS MIRI MRS pipeline v9.1 developed for the JWST JDISCS survey ([Arulanantham et al. 2025](#)).

We binned the spectra to a resolution of $R = 500$ ($\Delta\nu = 600 \text{ km s}^{-1}$), which is still much higher than that of SST IRS, to avoid issues with the Non-Negative Least-Squares (NNLS) calculation during the model fitting (as described in Section 3.3) due to the high spectral resolution. This resolution is sufficiently high to clearly capture the dust features described in Section 3.2, and was also adopted by [Jang et al. \(2024b\)](#), who studied the variability in PDS 70 based on the SST and JWST observations.

2.4 Spectra

The spectral data are shown in Fig. 1. In the following sections, we focus on the 5–25 μm range to compare the SST and JWST data. In the range of 5–7.5 μm , radiation from high-temperature optically thick components including the central star is observed, while amorphous silicate features from optically thin components are seen at longer wavelengths (e.g. the peak around 10 μm and the bumps at 18 μm). At longer wavelengths, sub-peaks characteristic of crystalline silicates can also be seen. These features have also been observed in other *T Tauri* stars (e.g. [Furlan et al. 2006](#)).

For both objects, the overall spectral shapes are similar between the SST and JWST spectra, but a temporal variation is clearly found. Sz 96 shows dimming at $\leq 18 \mu\text{m}$, while showing almost no variation at longer wavelengths. IP Tau brightens across the entire wavelengths, with a particularly strong enhancement around 10 μm . The flux differences reach 10–15% for Sz 96 and 30–35% for IP Tau.

3 FITTING

To investigate the temperature structure and dust composition of the discs, we performed model fitting to the spectral data. We used a model based on the Dust Continuum Kit (DuCK; [Kaeufer et al. 2024](#)), which was also employed in the analysis of SST and JWST spectral data for PDS 70 by [Jang et al. \(2024b\)](#). The model assumes contributions from several components: the central star, a vertically extended hot inner rim, the relatively cooler mid-plane of the disc, and the surface layer (see Fig. 2). While the inner rim and disc mid-plane are optically thick, the surface layer is optically thin. The emission from the optically thin surface produces the silicate features, and the model includes multiple species of silicate dust (see Section 3.2). The fitting parameters include the temperature, solid angle, and dust mass of each contributing component. In the original DuCK model, the surface layer and mid-plane have a radial temperature distribution. In the present study, however, we assume each component has a single temperature for simplicity. Although we also tried a model with radial temperature distributions, the quality of the fit did not significantly change. This minor modification does not affect the conclusions presented later in the paper. We performed the parameter fitting using our own Markov Chain Monte Carlo (MCMC) implementation, rather than the built-in nested sampling routine provided by DuCK.

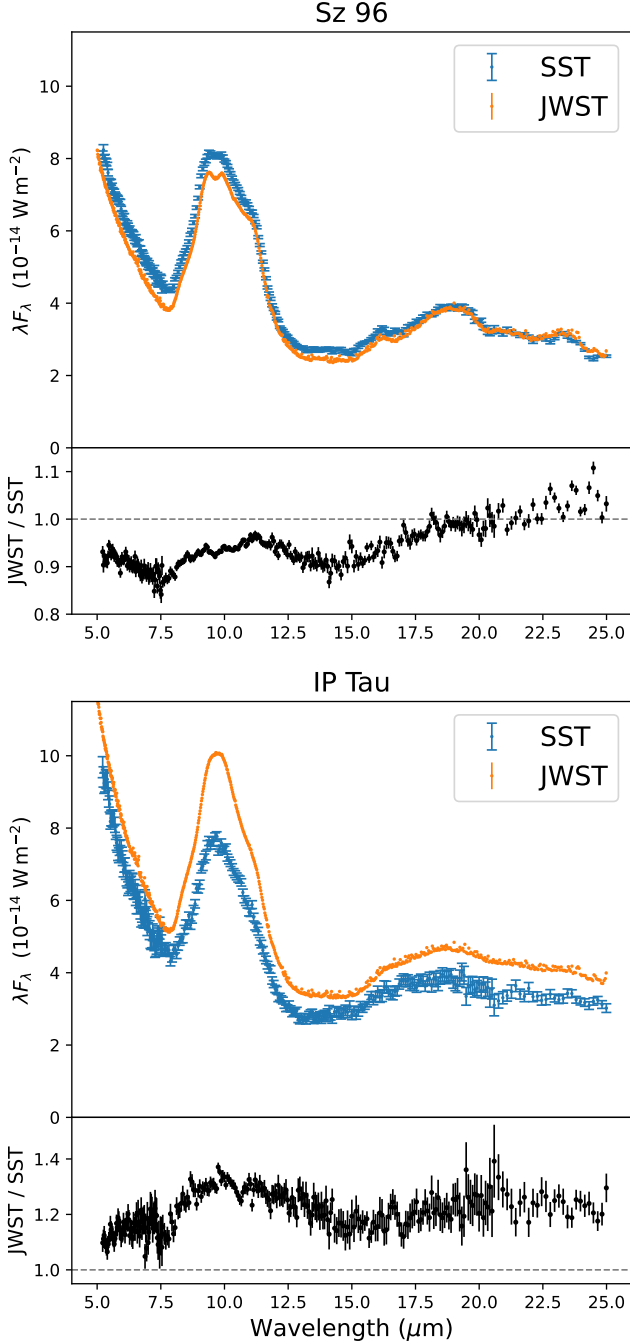


Figure 1. The SST (capped error bars) and JWST (vertical error bars) spectra and their ratio (JWST/SST) for Sz 96 (top) and IP Tau (bottom). The JWST data have been binned to a resolution of $R = 500$.

3.1 Model

The model spectrum is expressed as follows:

$$F_{\text{model}} = F_{\text{star}} + F_{\text{rim}} + F_{\text{mid}} + F_{\text{sur}}, \quad (1)$$

where F_{star} is the emission from the star, F_{rim} is from the inner rim, F_{mid} is from the mid-plane of the disc, and F_{sur} is from the optically thin surface layer.

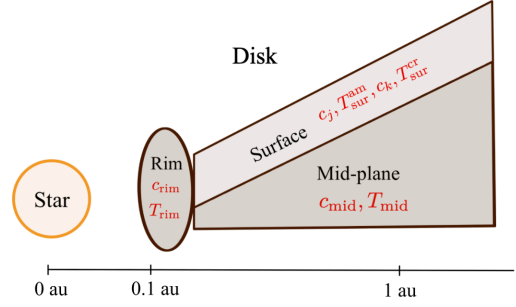


Figure 2. An illustration of the model used in our study. The star, rim and mid-plane are optically thick and the surface is optically thin. Silicate features are seen in the radiation from the surface.

The emission from the star is given by:

$$F_{\text{star}} = \frac{\pi R_{\text{star}}^2}{d^2} B(T_{\text{star}}), \quad (2)$$

where d is the distance to the star, R_{star} is the stellar radius, T_{star} is the stellar temperature, and $B(T)$ represents the Planck function with temperature T . We adopted the literature values listed in Table 1 for these parameters, and F_{star} is fixed in the model calculation.

The emission from the optically thick rim and mid-plane components is similarly expressed as:

$$F_{\text{rim}} = c_{\text{rim}} B(T_{\text{rim}}), \quad (3)$$

$$F_{\text{mid}} = c_{\text{mid}} B(T_{\text{mid}}), \quad (4)$$

where T_{rim} and T_{mid} are the temperatures of the rim and mid-plane, respectively. The parameters c_{rim} and c_{mid} correspond to the solid angles subtended by each radiation source as seen by the observer.

The emission from the optically thin surface layer is modelled by allowing two temperatures: one for amorphous grains ($T_{\text{sur}}^{\text{am}}$) and one for crystalline grains ($T_{\text{sur}}^{\text{cr}}$). The total surface emission is then given by:

$$F_{\text{sur}} = \sum_j c_j \kappa_j B(T_{\text{sur}}^{\text{am}}) + \sum_k c_k \kappa_k B(T_{\text{sur}}^{\text{cr}}), \quad (5)$$

where j and k represent the amorphous and crystalline silicate dust species included in the model, and κ is the mass absorption coefficient. We note that scattering is negligible in the optically thin surface layer (Jang et al. 2024b). In this formulation, c is proportional to the dust mass present in the surface layer.

Although our model assumes a constant stellar flux, we note that both objects can show optical variability that may be related to dipper-like extinction events. However, since the extinction efficiency decreases rapidly toward the mid-infrared, for instance, Wang & Chen (2019) report $A_{\lambda}/A_V = 0.026$ at $\lambda = 4.5 \mu\text{m}$, the corresponding flux change would be negligible. Therefore, the assumption is not expected to introduce significant uncertainty in our analysis.

3.2 Dust mass absorption coefficient

We considered five dust species in the model following Jang et al. (2024b): amorphous forsterite, amorphous enstatite, amorphous silica, crystalline forsterite, and crystalline enstatite. For each species, grain sizes of 0.1, 2, and $5 \mu\text{m}$ were adopted following Juhász et al. (2010). We tested 6 grain sizes (0.1, 1, 2, 3, 4, and $5 \mu\text{m}$) as in Jang et al. (2024b), but found that the fitting quality did not improve significantly. Therefore, we adopted the 3 grain sizes for simplicity. These sizes are typical in protoplanetary discs, and grain sizes greater than

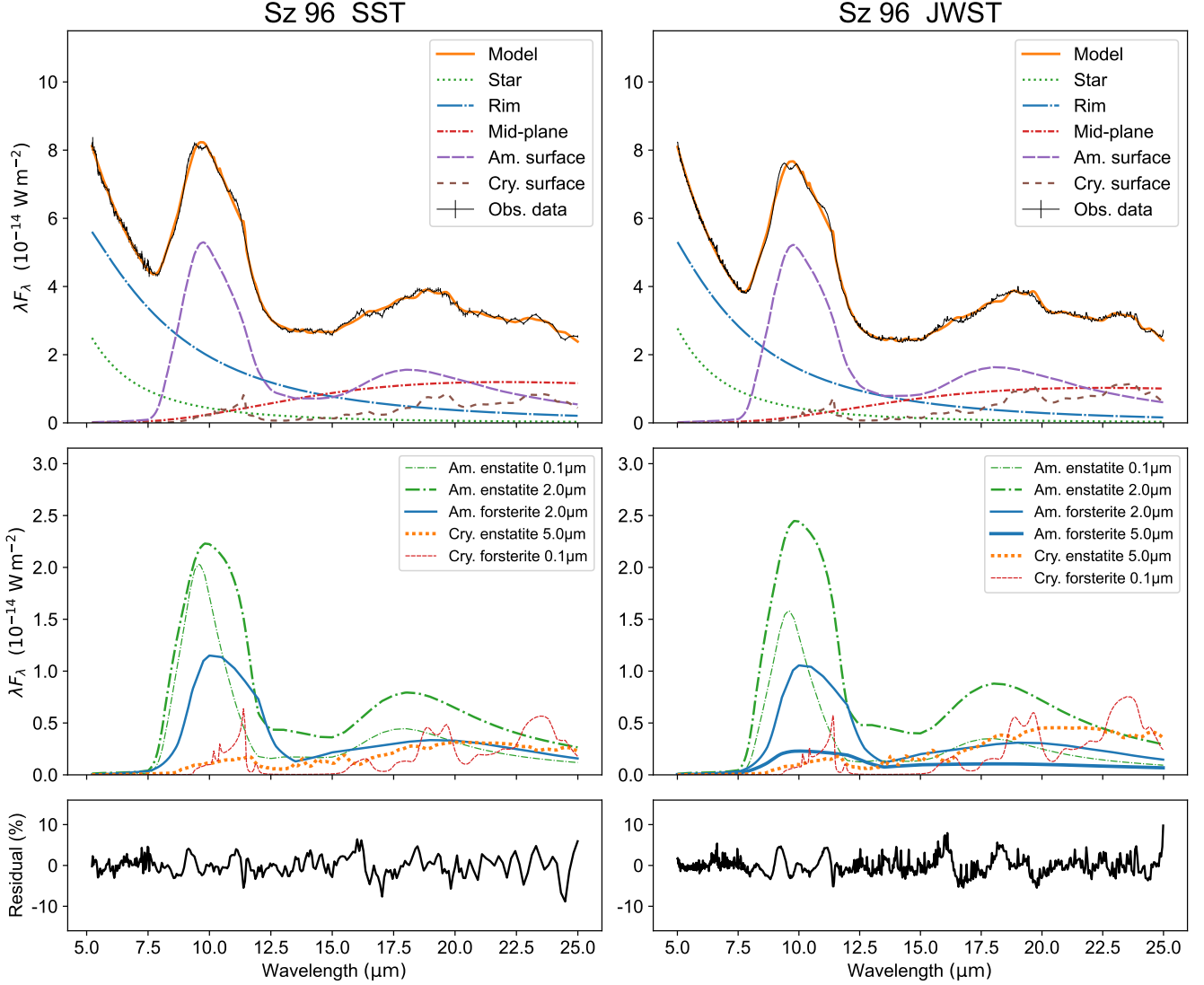


Figure 3. Fitting results of Sz 96: overall fitting results (top), contributions from each dust component (middle), and residual of the best-fitting model (bottom) for SST (left) and JWST (right). In the middle panel, the emissions from the star, rim, and mid-plane, as well as components contributing less than 0.5% to the total flux, are not shown.

5 μm are not considered because the band strength becomes very weak already for 5 μm -sized grains (Jang et al. 2024b). The optical constants of each dust species were obtained from the literature listed in Table 2. The mass absorption coefficients were calculated using the optical constants with the Python package *Optool* (Dominik et al. 2021). We employed the Distribution of Hollow Spheres (DHS; Min et al. 2003) model in *Optool*, which calculates the average optical properties of dust aggregates with complex shapes by approximating them as hollow spheres. This statistical approach avoids the artificial resonances associated with idealized spherical grains and provides a more realistic representation of the optical properties of irregular and porous dust particles in protoplanetary discs (Min et al. 2016; Woitke et al. 2016). The parameter f_{max} , representing the hollow fraction, was set to $f_{\text{max}} = 0.7$ for amorphous dust and $f_{\text{max}} = 0.99$ for crystalline dust, as these values are appropriate for reproducing the features of each dust type (Min et al. 2005; Min et al. 2007). The optical properties of crystalline silicates depend on the relative ori-

entation between the incident radiation field and the crystallographic axes. Two approaches can be used to calculate the absorption coefficient taking into account the anisotropy of the refractive index. One is the Bruggeman rule, which treats each grain as an ensemble of sub-wavelength crystalline domains that are randomly oriented within the particle, thereby deriving an effective dielectric response for the grain as a whole (Bruggeman 1935). The other is the three-axis average, which treats each grain as a single crystal and computes the absorption along the three principal crystallographic axes, then averages these values assuming a random orientation of the grains. In this study, we adopted the Bruggeman rule, and the results are presented in Section 4. We also tested the simple averaging method, and the results are shown in Appendix A.

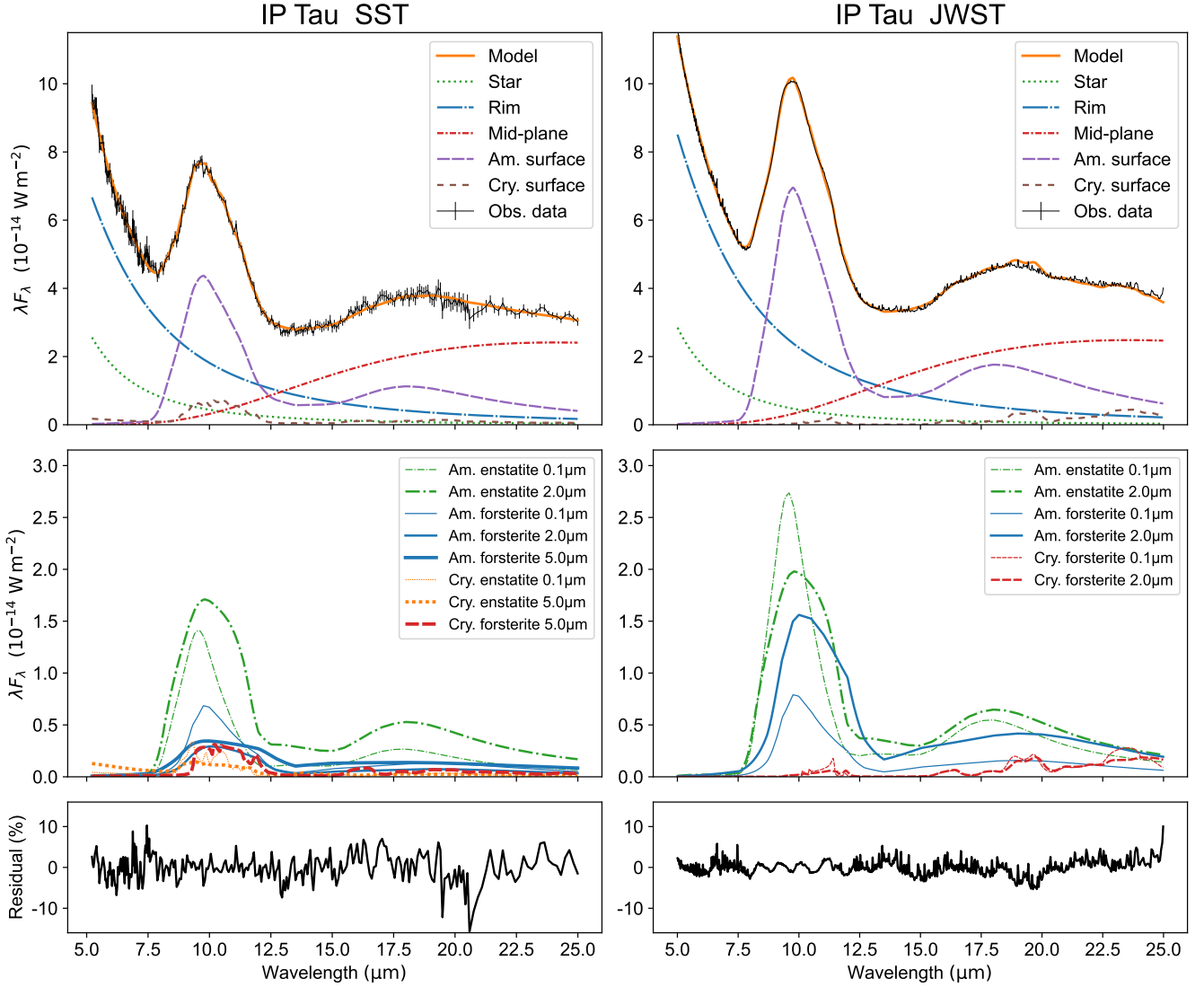


Figure 4. Fitting results of IP Tau: overall fitting results (top), contributions from each dust component (middle), and residual of the best-fitting model (bottom) for SST (left) and JWST (right). In the middle panel, the emissions from the star, rim, and mid-plane, as well as components contributing less than 0.5% to the total flux, are not shown.

Table 2. The references of optical constants to calculate the mass absorption coefficients.

Species	Reference
Amorphous forsterite	Jäger et al. (2003)
Amorphous enstatite	Dorschner et al. (1995)
Amorphous silica	Kitamura et al. (2007)
Crystalline forsterite	Suto et al. (2006)
Crystalline enstatite	Jaeger et al. (1998)

3.3 Fitting

The fitting parameters are the temperatures T and coefficients c of each component, making a total of 21 parameters. In this fitting, we combined the MCMC method with the NNLS method. First, MCMC proposes a set of four temperatures (T_{rim} , T_{mid} , $T_{\text{sur}}^{\text{am}}$, and $T_{\text{sur}}^{\text{cr}}$). For

the given temperatures, the set of c values that best matches the observational data is computed by NNLS. Once the parameter set is determined, the model spectrum can be computed, and the likelihood, expressed by the following equation, can be calculated:

$$\mathcal{L} = \prod_{i=1}^{N_{\text{obs}}} \frac{1}{\sqrt{2\pi}\sigma_i} \exp \left[-\frac{(F_{\text{model},i} - F_{\text{obs},i})^2}{2\sigma_i^2} \right], \quad (6)$$

where i represents each data point, and σ is the uncertainty in the observational data. This allows the MCMC process to proceed to the next step using the updated temperature parameters. We set the prior ranges for the temperature of the rim, mid-plane, amorphous and crystalline dust in the surface to be $T_{\text{rim}} = [500, 1900]$ K, $T_{\text{mid}} = [10, 700]$ K, $T_{\text{sur}}^{\text{am}} = [10, 1000]$ K, and $T_{\text{sur}}^{\text{cr}} = [10, 1500]$ K, respectively. For the MCMC method, we used the Python package *emcee* (Foreman-Mackey et al. 2013), and for the NNLS method, we used the *nnls* function in the *SciPy* (Virtanen et al. 2020) library. In *emcee*, the number of walkers and steps were set to 32 and 5000, respec-

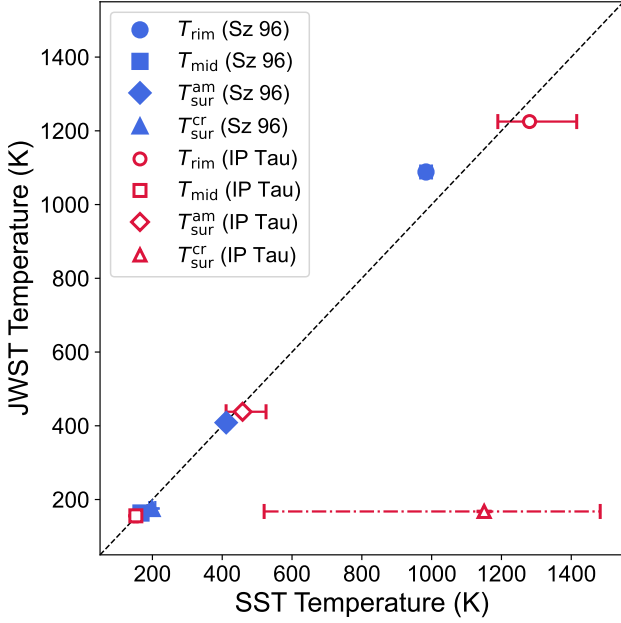


Figure 5. The temperature parameters for Sz 96 (filled symbols) and IP Tau (open symbols). The x-axis represents SST temperatures, while the y-axis represents JWST temperatures. The error bars represent the 0.025 and 0.975 quantiles of the posterior distributions of the parameters. The dashed line shows where the SST and JWST temperatures would be equal. $T_{\text{sur}}^{\text{cr}}$ for the SST data of IP Tau is unconstrained.

tively, and the default StretchMove with the stretch scale parameter $a = 2.0$ was used (Goodman & Weare 2010). The fitting was performed independently for the SST and JWST data.

4 RESULTS

The fitting results for Sz 96 and IP Tau are presented in Figs 3 and 4, respectively. The medians of the posterior distributions of the fitting parameters, together with the RMS residuals of the best-fitting models for each spectrum, are summarised in Table 3.

The top panels of Fig. 3 show that Sz 96 exhibits a decrease in the emission from the rim, whereas the mid-plane and surface components exhibit no significant variations in the JWST data compared with the SST data. In the middle panels, the observed features around $10 \mu\text{m}$ are dominated by amorphous silicates and are well reproduced by a combination of amorphous forsterite and enstatite with grain sizes of 0.1, 2, and $5 \mu\text{m}$. The features around $20 \mu\text{m}$ are reproduced by the emission features of crystalline forsterite grains with sizes of $0.1 \mu\text{m}$ and crystalline enstatite grains with a size of $5.0 \mu\text{m}$ in addition to the amorphous silicates. Despite small differences in the best-fitting grain sizes, we do not interpret these as meaningful changes in the grain size distribution between the two epochs, as the spectral features of each dust species included in the best-fitting model do not change significantly with grain size. The RMS residual is 2.2% for the SST data and 2.0% for the JWST data.

For IP Tau, the top panels of Fig. 4 show that the rim and the surface components become brighter, while the mid-plane component exhibits no significant change in the JWST data. For the SST data, $T_{\text{sur}}^{\text{cr}}$ is unconstrained (see Appendix B). Since the posterior of $T_{\text{sur}}^{\text{cr}}$ is biased toward higher temperatures, we set $T_{\text{sur}}^{\text{cr}} = T_{\text{rim}} = 1281 \text{ K}$

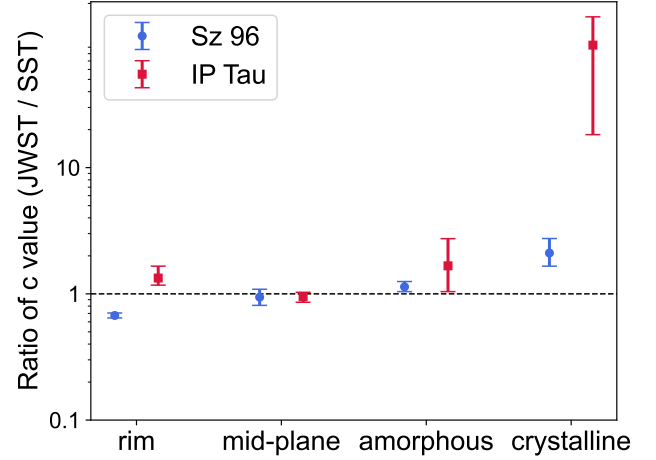


Figure 6. The ratio of the c value (JWST/SST) for Sz 96 (circles) and IP Tau (squares). The error bars represent the 0.025 and 0.975 quantiles of the ratio, computed using samples drawn from the posterior distributions of the c values for the JWST and SST data. The c value for each component represents the solid angle as seen by the observer for the rim and mid-plane, and the dust mass in the surface region for amorphous and crystalline components.

in the best-fitting model in Fig. 4 for practical purposes, although all subsequent discussions of the variability are based on the values listed in Table 3. The SST data show that the features around $10 \mu\text{m}$ are reproduced by the amorphous forsterite and enstatite grains with sizes of 0.1, 2, and $5 \mu\text{m}$, and the crystalline forsterite and enstatite with sizes of 0.1 and $5 \mu\text{m}$. In contrast, those in the JWST data are mainly reproduced by amorphous forsterite and enstatite with grain sizes of 0.1 and $2 \mu\text{m}$. The features around $20 \mu\text{m}$ in the JWST data are reproduced by crystalline forsterite grains with sizes of 0.1 and $2 \mu\text{m}$ in addition to the amorphous silicates, as in Sz 96. The RMS residual is 3.3% for the SST data and 1.6% for the JWST data.

The temperatures of disc components for Sz 96 and IP Tau are shown in Table 3 and Fig. 5. For Sz 96, the rim temperature increases by 104 K, whereas the surface crystalline component varies by 23 K, and the surface amorphous dust and mid-plane shows no significant change. In the case of IP Tau, no significant changes in the temperature parameters are found in the JWST data compared to the SST data except for $T_{\text{sur}}^{\text{cr}}$. The mean of the posterior distribution for $T_{\text{sur}}^{\text{cr}}$ (1150 K) in the SST data of IP Tau should not be interpreted as the best-fitting value. The posterior distribution has a lower bound at 300 K, with no samples found below this value.

Interestingly, in both the SST and JWST data of Sz 96, as well as in the JWST data of IP Tau, the temperature of the crystalline component is currently as low as 170–200 K, and lower than that of the amorphous silicates (410–460 K). Crystallisation is understood to occur through high-temperature annealing ($\geq 1000 \text{ K}$). If the lower temperature obtained in this analysis has always been representative of the crystalline component, it is consistent with the possibility that re-amorphisation operates in the inner disc and crystalline silicates are transported to larger radii. This is discussed in further detail in Section 5.2.

The ratios of the c values in the model of the JWST data to those of the SST data are shown in Fig. 6. The c values for the amorphous and crystalline dust represent the sum over each type of dust component. The c values for the rim and mid-plane represent the emitting area of the rim and mid-plane, respectively, while the c values for the

Table 3. The medians and the 0.025 and 0.975 quantiles of the posterior distributions of the parameters and the RMS residual for each spectrum. The parameter $c_{\text{sur}}^{\text{am}}$ and $c_{\text{sur}}^{\text{cr}}$ represent the sum over each type of dust component. The units of c parameters are 10^{-18} sr for the rim, 10^{-15} sr for the mid-plane, and 10^{-20} g cm $^{-2}$ sr for the surface components.

Target	Data	T_{rim} (K)	T_{mid} (K)	$T_{\text{sur}}^{\text{am}}$ (K)	$T_{\text{sur}}^{\text{cr}}$ (K)	c_{rim}	c_{mid}	$c_{\text{sur}}^{\text{am}}$	$c_{\text{sur}}^{\text{cr}}$	Residual (RMS)
Sz 96	SST	984 $^{+17}_{-16}$	167 $^{+4}_{-4}$	411 $^{+10}_{-9}$	199 $^{+9}_{-8}$	5.4 $^{+0.2}_{-0.2}$	1.2 $^{+0.2}_{-0.2}$	4.7 $^{+0.4}_{-0.4}$	17 $^{+5}_{-4}$	2.2%
	JWST	1088 $^{+0.6}_{-0.6}$	163 $^{+0.2}_{-0.2}$	409 $^{+0.3}_{-0.3}$	176 $^{+0.2}_{-0.2}$	3.6 $^{+0.01}_{-0.01}$	1.1 $^{+0.01}_{-0.01}$	5.3 $^{+0.02}_{-0.02}$	36 $^{+0.3}_{-0.3}$	2.0%
IP Tau	SST	1281 $^{+135}_{-91}$	153 $^{+4}_{-5}$	458 $^{+67}_{-47}$	1150 $^{+333}_{-630}$	3.2 $^{+0.4}_{-0.6}$	3.4 $^{+0.4}_{-0.3}$	3.0 $^{+0.2}_{-0.1}$	0.1 $^{+0.4}_{-0.04}$	3.3%
	JWST	1225 $^{+0.6}_{-0.6}$	156 $^{+0.06}_{-0.04}$	438 $^{+0.3}_{-0.3}$	168 $^{+0.8}_{-0.7}$	4.2 $^{+0.01}_{-0.01}$	3.1 $^{+0.01}_{-0.01}$	5.0 $^{+0.01}_{-0.01}$	9.5 $^{+0.23}_{-0.19}$	1.6%

surface amorphous and crystalline dust represent the dust mass in the surface region. For Sz 96, the c value for the rim decreases by 33%, while that for the mid-plane does not change significantly and the amorphous and crystalline dust in the surface increase by 13% and 112%, respectively. In IP Tau, the c value for the rim and the amorphous dust increase by 31% and 67%, respectively. The c value for the crystalline dust in the surface shows a significant increase, although with large uncertainty due to the unconstrained $T_{\text{sur}}^{\text{cr}}$.

For the JWST fits, the estimated parameter uncertainties $\approx 0.1\%$ are much smaller than the residuals $\approx 2\%$. This is because the parameter uncertainties reflect the local curvature of the χ^2 surface around its minimum, rather than the overall goodness of fit. Consequently, they are primarily governed by the statistical uncertainties of the data. The statistical uncertainties of the JWST spectra, which include photon Poisson noise and detector read noise and correspond to a signal-to-noise ratio ≈ 1000 , are responsible for the small parameter uncertainties. The larger residuals likely arise from systematic uncertainties and physical components not captured by the current model.

The results using the simple averaging method for crystalline silicates optical properties (see Section 3.2) are presented in Appendix A. The variabilities of the model parameters for IP Tau are consistent. However, for Sz 96, the variability of the T and c parameters for the mid-plane and crystalline surface components is opposite to that presented in Section 4, as discussed in Appendix A. Therefore, we note that the interpretation of the c variability of the mid-plane and crystalline surface components discussed in Section 5.3 is not robust, as it may depend on the method used to combine the refractive index data for crystalline silicates.

5 DISCUSSION

5.1 The discrepancy between the best-fitting model and the observed data

The current model successfully reproduces the overall shapes of the mid-infrared spectra, but a closer inspection reveals discrepancies between the model spectrum and the observed data, particularly for Sz 96, where more distinct spectral features are observed compared to IP Tau. In the case of JWST data of Sz 96, for example (Fig. 7), the main discrepancies are as follows: (1) two broad bumps in the 9–10 μm region in the observed data, which are not captured by the model, (2) two peaks in the 10–10.5 μm region in the model, which are not observed, and (3) a mismatch in the shoulder feature around 11 and 18 μm .

Regarding (1), these bumps could be reproduced by crystalline enstatite features. However, its contribution in the best-fitting model is limited to a level too small to account for the two bumps. While

the features in the 9–10 μm region could be reproduced by allowing a higher temperature for crystalline enstatite, we do not consider this possibility, because assuming different temperatures for crystalline forsterite and enstatite would be unrealistic.

(2) and (3) may be attributed to shape effects used to calculate the dust mass absorption coefficients in the model. While we adopted the DHS approach in this study, Jang et al. (2024b) used different methods, including Gaussian Random Field (GRF; Min et al. 2007) method and laboratory aerosol measurements (Tamanai et al. 2006). These alternative models may reproduce the observed features but they may fail to reproduce the features beyond 20 μm that are well matched by the DHS model used in this study (see Section 5.2 and fig. 2 in Jang et al. 2024b).

Although minor discrepancies remain as described above, no further tuning was performed, as the fits are very good and the mismatches result in only local and small residuals of less than 5%.

5.2 Temperature of crystalline silicate

As discussed in Section 4, in the SST and JWST data of Sz 96 and the JWST data of IP Tau, the crystalline silicates are found at lower temperatures than the amorphous component. This result arises from the attempt to reproduce the spectra, where crystalline features are prominent at ~ 18 μm but weaker at ~ 10 μm . To verify the robustness of this result, we performed a fitting analysis on the JWST data of Sz 96 using a modified model in which the crystalline and amorphous components were constrained to have the same temperature. We define the original model as Model A and the modified model with the temperature constraint as Model B. The best-fitting spectra for each model are shown in Fig. 7. The RMS residual is significantly larger for Model B than for Model A, with the values of 2.035(1)% and 2.692(3)%, respectively, where the values in parentheses indicate 3σ uncertainties. This trend becomes more evident at wavelengths longer than 20 μm ; 2.579(3)% for Model A and 4.055(6)% for Model B. While the reproduced spectra around 10 μm are almost the same, the crystalline feature around 20 μm is better reproduced by Model A than by Model B. We thus conclude that our finding of lower temperature of crystalline silicates than that of the amorphous component is robust.

Similar results have been reported in several studies using SST data of T Tauri stars. Bouy et al. (2008) modelled the SST IRS data of T Tauri stars and confirmed that the crystalline fraction in the cooler components (130 K) was 10–15 times higher than that in the warmer components (270 K). Olofsson et al. (2009) analysed the spectra of 108 T Tauri stars observed as part of the c2d Spitzer legacy programme (Evans et al. 2003), and found that crystalline features were detected 3.5 times more frequently in the wavelength range $\lambda > 20$ μm compared to $\lambda < 10$ μm . However, Olofsson et al. (2010) proposed that in regions with a low crystalline fraction (i.e. the hotter

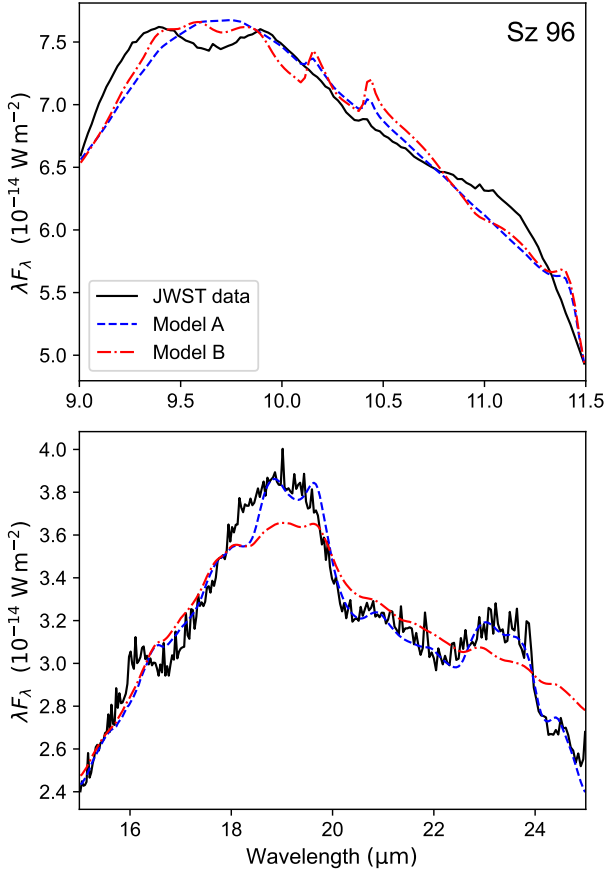


Figure 7. Best fit for JWST MIRI MRS data of Sz 96. Model A (dashed curve) allows different temperatures for amorphous and crystalline components, while their temperatures are set to be the same in Model B (dash-dotted curve). The top panel shows an enlarged plot around $10 \mu\text{m}$, and the bottom panel shows an enlarged plot around $20 \mu\text{m}$. The best-fitting values of the T parameters for model B are $T_{\text{rim}} = 1089 \text{ K}$, $T_{\text{mid}} = 130 \text{ K}$, and $T_{\text{sur}} = 406 \text{ K}$.

components), crystalline features are buried in the amorphous features due to contrast issues. In the present study, using the JWST MIRI MRS data with higher spectral resolution and signal-to-noise ratio compared to the SST IRS data should make the crystalline features much clearer. Thus, our analysis of the JWST spectra suggests that the crystalline features are more prominent at longer wavelengths than at shorter wavelengths, which is not due to contrast issues.

The fact that crystals exist at lower temperatures suggests that they are located in the outer regions of the disc. However, crystalline silicates are generally believed to be localised in the innermost part of the disc or on the disc surface near the central star, where crystallisation efficiently occurs via annealing (Jang et al. 2024a). The mechanism that leads to the presence of crystalline silicates in the outer region is under debate. Gail (2004) suggested that material in the inner disc is heated and processed as it moves inward within the disc, and partially redistributed to the outer disc through turbulence and circulation. Giacalone et al. (2019) showed that magnetocentrifugally driven disc winds can uplift submicron- to micron-sized crystalline grains from the inner disc surface and allow them to re-enter the disc at larger radii. Their model demonstrates that $1 \mu\text{m}$ -sized crystalline grains at $\sim 0.1 \text{ au}$ can be transported outward and re-enter the disc at distances of $1\text{--}10 \text{ au}$. Jang et al. (2024a) also proposed the fol-

lowing hypothesis: in the inner region of the disc, the crystallised silicates are easily re-amorphised by high-energy particles and cannot survive, thus crystalline silicates are found in the relatively outer, low-temperature region. Existing measurements show that Sz 96 has a typical X-ray luminosity of $\sim 3.1 \times 10^{30} \text{ erg s}^{-1}$ (Gardner et al. 2006), while no published X-ray luminosity is available for IP Tau. The re-amorphisation process by high-energy particles was quantitatively evaluated by Glauser et al. (2009). The relationship between crystalline fraction and X-ray luminosity, which can trace stellar activity and energetic ions from stellar winds, was investigated based on model fitting to SST/IRS data of T Tauri stars, but no statistically significant correlation was found (Olofsson et al. 2010). Identifying the mechanism requires detailed modelling of mixing due to disc winds and re-amorphisation. Nevertheless, the fact that we obtain consistent results with previous studies even using JWST data, which reveal crystalline features more clearly than before, highlights the robustness of this trend.

For the SST data of IP Tau, the posterior distribution of $T_{\text{sur}}^{\text{cr}}$ is broad and lacks a clear peak due to the low signal-to-noise ratio of the data, spanning from $\sim 300 \text{ K}$ to the edge of the prior range at 1500 K . Even when the prior range is extended, the posterior distribution correspondingly broadens toward higher temperatures. This may indicate the presence of high-temperature crystalline dust located in the inner disc of IP Tau, although both the SST and JWST spectra around $10 \mu\text{m}$ do not show corresponding crystalline dust features. Given that the best-fitting model for the JWST data yields no contribution from crystalline enstatite components, we also performed the same analysis on the SST data with crystalline enstatite excluded. The result shows that the posterior distributions of T_{rim} , T_{mid} , $T_{\text{sur}}^{\text{am}}$, and $T_{\text{sur}}^{\text{cr}}$ have peaks at 1307 , 157 , 408 , and 38 K , respectively, resulting in a lower temperature for the crystalline dust. The fit quality does not change significantly when crystalline enstatite is included: the mean absolute residual is $3.27(7)\%$ for the model without crystalline enstatite and $3.32(8)\%$ for the model including crystalline enstatite, where the values in parentheses indicate 3σ uncertainties. Thus, we caution that the temperature and mass of the crystalline dust in the SST data of IP Tau are highly uncertain and sensitive to the choice of crystalline species included in the model. Therefore, we exclude the variability of crystalline dust of IP Tau from the discussion in Section 5.3.

5.3 Mechanism of Variability

In the present study, the time variation of the spectra is analysed for two T Tauri stars with different disc structures, covering temporal baselines of 18 years for Sz 96 and 16 years for IP Tau. Here, we discuss the mechanism of the variability with a simple model. The reference model is the one proposed by Espaillat et al. (2011). They explained the variability of a pre-transitional disc by changing the scale height of the inner disc. Based on this idea, we discuss the possibility that the observed spectral changes are caused by structural changes in the inner region of the discs. In addition, a disc structure with crystalline dust in the outer region is assumed (Section 5.2).

Sz 96 has a full disc, as suggested by its infrared excess. Based on our fitting results, the emitting area of the rim decreases, while that of the mid-plane shows no significant change, and the mass of the surface amorphous and crystalline dust increase. This variability can be explained by a reduction in the disc scale height in the inner region. We illustrate the proposed scenario in detail in Fig. 8. We consider a disc structure in which the innermost region contains the rim, followed by a surface region with amorphous dust and the mid-plane that lies at the bottom of the optically thin layer. In the outer colder

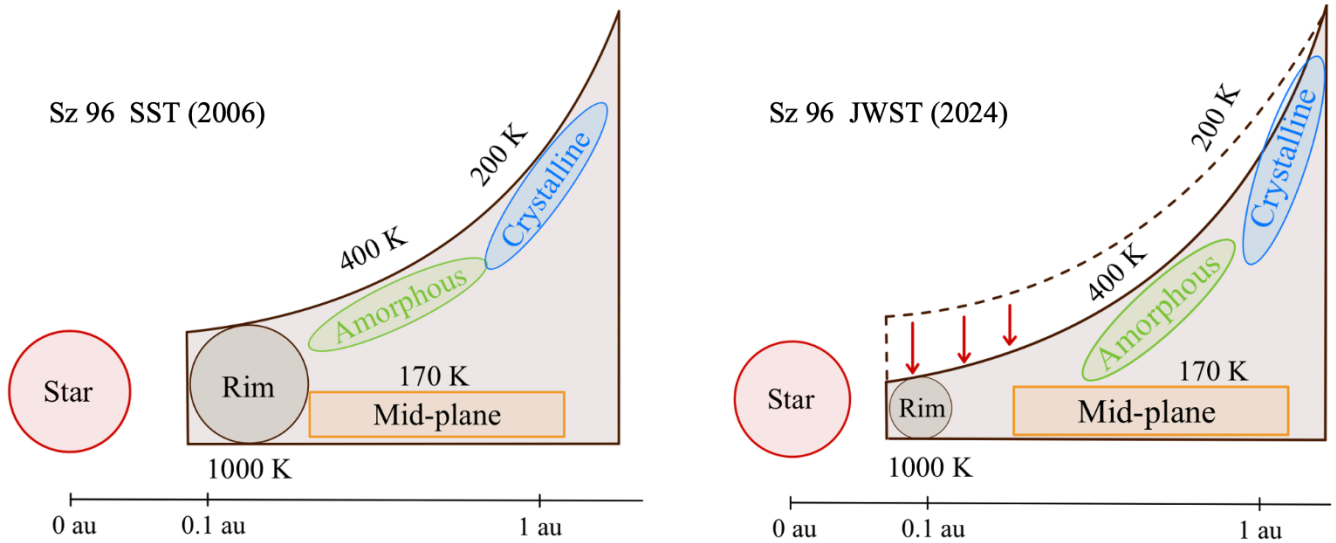


Figure 8. Changes in the disc structure which explain the variability of Sz 96 between the SST (left) and JWST (right) observations. As the scale height of the inner region of the disc decreases, the rim becomes smaller, and both the amorphous and crystalline surface experience an increase in the solid angle as seen from the central star, leading to an increase in the input energy.

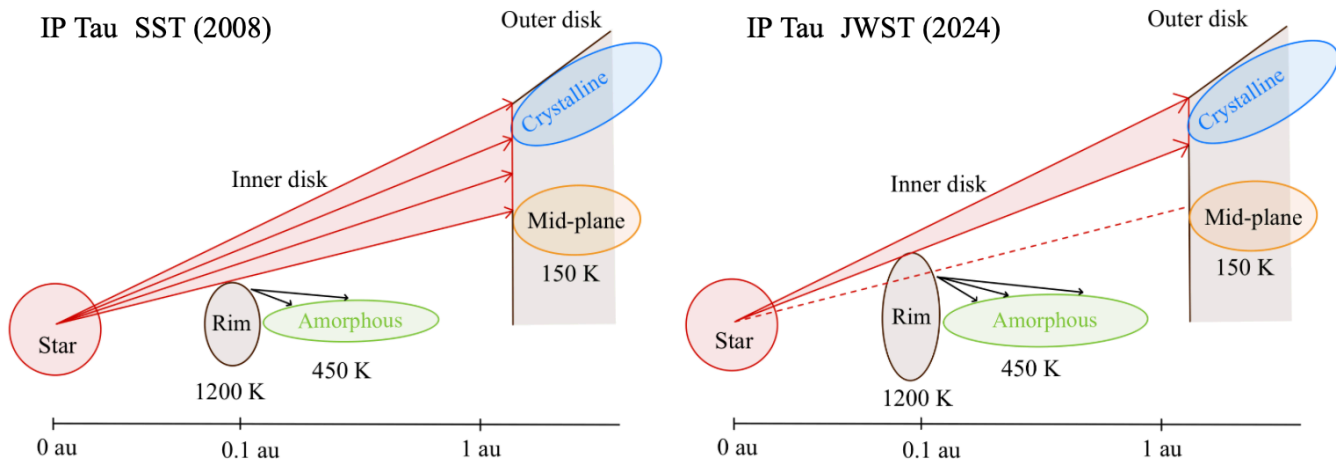


Figure 9. Changes in the disc structure which explain the variability of IP Tau between the SST (left) and JWST (right) observations. As the height of the rim at the inner disc becomes larger, the amorphous dust gains more input energy from the rim and the outer disc is shadowed (Espaillat et al. 2011).

regions, a surface layer of crystalline dust is present. Although the rim temperatures in the SST and JWST models are similar, the scale height can differ because it is governed by the mid-plane temperature, which is not directly constrained. Vertical mixing within the inner rim, for example induced by magnetically driven turbulence (Flock et al. 2017), can modify its internal vertical temperature structure and thereby lead to variations in the rim height. As the scale height of the inner disc becomes smaller, the vertical extent of the rim decreases and the rim subtends a smaller solid angle toward the observer. At the same time, a reduced rim allows a larger fraction of stellar radiation to reach the disc surface. Consequently, the surface layer containing amorphous and crystalline silicates intercepts more stellar energy, increasing the amount of dust that emits in the mid-infrared.

The disc around IP Tau is classified as a pre-transitional disc. Our analysis shows that the emitting area of the rim increases while that

of the mid-plane does not change significantly, whereas the mass of the amorphous dust in the surface increases in the JWST data compared with the SST data. This variability can be explained by an increase in the scale height of the inner disc, which casts a larger shadow over the outer disc (Espaillat et al. 2011; see Fig. 9). The assumed disc structure consists of the inner disc rim, a gap with optically thin amorphous dust, and the outer disc with a surface layer of cold crystalline dust and the mid-plane at its base. This structure was proposed by Espaillat et al. (2011) to explain the strong $10\ \mu\text{m}$ silicate emission feature of pre-transitional discs including IP Tau. The inner disc rim expands its emitting area from the SST era to the JWST era. As the rim becomes larger, the amorphous dust that mainly receives radiation from the rim gains more input energy, increasing the mass of dust emitting in the mid-infrared. Simultaneously, the larger shadow cast on the outer disc can reduce the mid-plane emitting

area, but because the mid-plane constitutes the base of the disc, the decrease is slight and not significant.

These scenarios explain all of the observed temporal variations as resulting from changes in the disc structure. However, the observed changes in the dust mass may alternatively arise from dust clouds lifted into the disc atmosphere via turbulence, and this possibility cannot be excluded. Although the model used in this study successfully reproduces the mid-infrared spectra with a small number of parameters, it is based on a simple spectral decomposition and does not explicitly account for the detailed disc structure. Therefore, the structural changes inferred from variations in the model parameters involve inherent ambiguities. The next step in uncovering the full nature of the dust disc is to construct models that incorporate the overall disc geometry and are consistent with the full spectral energy distribution.

6 CONCLUSIONS

We analysed mid-infrared spectra of two T Tauri stars, Sz 96 and IP Tau, obtained by SST and JWST. The spectra were fitted by a model that separates the emission into optically thin and thick components. The optical properties of crystalline silicates were primarily calculated using the Bruggeman rule, while the simple averaging method was also tested for comparison. We quantitatively evaluated the variability of the dust composition and temperature distribution of the discs over approximately 20 years between the SST and JWST observations. From these results, we derived the following three conclusions.

(i) In the disc around Sz 96, the emitting area of the rim decreases, while that of the mid-plane does not change significantly. The dust mass in the surface increases for both amorphous and crystalline components. However, we found that the variability of the mid-plane and crystalline dust become opposite when using the simple averaging method. In the disc around IP Tau, the emitting area of the rim increases while that of the mid-plane does not change significantly, whereas the amorphous dust mass increases. The variability of the crystalline dust in the surface of IP Tau cannot be reliably determined, as it strongly depends on the dust species included in the model. These variabilities for IP Tau are consistent regardless of the method used to calculate the optical properties of crystalline silicates.

(ii) The observed spectral variations may be qualitatively explained by the change in the scale height of the inner region of the discs. The temporal variation is different in Sz 96 and IP Tau, which may also be explained by their different disc structures. Further studies with self-consistent models of disc structure and radiation transfer are desirable. The longer time baseline observation would help determine whether the observed rim size variations are part of transient events or indicative of secular structural evolution. Future JWST monitoring over several years would provide valuable constraints on the time-scales and physical drivers of these structural changes.

(iii) The temperature of crystalline silicates is lower than that of amorphous silicates in the SST and JWST data of Sz 96 and the JWST data of IP Tau. Although it was suggested in the SST observations of some discs, the higher spectral resolution and sensitivity of JWST robustly establish this finding. This suggests that crystalline silicates are depleted in the hot inner disc, which could be due to re-amorphisation in the inner disc or transportation to outer radii by disc winds.

ACKNOWLEDGEMENTS

T.M. acknowledges the support by KAKENHI grant number 23K20237. Y.A. acknowledges the support by KAKENHI grant number 24K00674 and 20H05847. T.J.H. acknowledges a Dorothy Hodgkin Fellowship, UKRI guaranteed funding for a Horizon Europe ERC consolidator grant (EP/Y024710/1) and UKRI/STFC grant ST/X000931/1. C.J.L. acknowledges the support by NASA through the NASA Hubble Fellowship grant No. HST-HF2-51535.001-A awarded by the Space Telescope Science Institute, which is operated by the Association of Universities for Research in Astronomy, Inc., for NASA, under contract NAS5-26555. N.P.B. acknowledges support from NSF grant No. AST-2205698 and NASA/Space Telescope Science Institute grants JWST-GO-03271 and JWST-GO-05460. C.G.R. acknowledges support from ANID-Millennium Science Initiative Program-Center Code NCN2024 001. V.V.G. acknowledges support from ANID-Millennium Science Initiative Program-Center Code NCN2024_001, CATA-Basal FB210003 and from FONDECYT Regular 1221352. We acknowledge Klaus M. Pontoppidan for his reduction of the JWST data, and Gianni Cataldi for his valuable guidance on MCMC sampling. This research has made use of the NASA/IPAC Infrared Science Archive, which is operated by the Jet Propulsion Laboratory, California Institute of Technology, under contract with the National Aeronautics and Space Administration. This work is based on observations made with the Spitzer Space Telescope, which was operated by the Jet Propulsion Laboratory, California Institute of Technology under a contract with NASA. This work is based on observations made with the NASA/ESA/CSA James Webb Space Telescope. The data were obtained from the Mikulski Archive for Space Telescopes at the Space Telescope Science Institute, which is operated by the Association of Universities for Research in Astronomy, Inc., under NASA contract NAS 5-03127 for JWST. These observations are associated with programme #50403. The authors declare no conflicts of interest.

DATA AVAILABILITY

The JWST MIRI MRS data used in this study are accessible from the Mikulski Archive for Space Telescopes (MAST³) as part of the programme 3228 (PI: L. Ilseadore Cleaves). The SST IRS data for Sz 96 and IP Tau were retrieved from the NASA/IPAC Infrared Science Archive (IRSA⁴) as part of the IRS Enhanced Spectrophotometric Products. Sz 96 was observed under programme 179 (PI: Neal Evans), and IP Tau under programme 50403 (PI: Nuria Calvet).

REFERENCES

- Alcalá J. M., et al., 2017, *Astronomy & Astrophysics*, 600, A20
 Alencar S. H. P., et al., 2010, *Astronomy & Astrophysics*, 519, A88
 Argyriou I., et al., 2023, *Astronomy & Astrophysics*, 675, A111
 Arulanantham N., et al., 2025, *The Astronomical Journal*, 170, 67
 Bellm E. C., 2014, The Zwicky Transient Facility ([arXiv:1410.8185](https://arxiv.org/abs/1410.8185)), [doi:10.48550/arXiv.1410.8185](https://doi.org/10.48550/arXiv.1410.8185)
 Bockelée-Morvan D., Gautier D., Hersant F., Huré J.-M., Robert F., 2002, *Astronomy & Astrophysics*, 384, 1107
 Bouy H., et al., 2008, *Astronomy & Astrophysics*, 486, 877
 Bredall J. W., et al., 2020, *Monthly Notices of the Royal Astronomical Society*, 496, 3257

³ <https://archive.stsci.edu/missions-and-data/jwst>

⁴ <https://irsa.ipac.caltech.edu/frontpage/>

- Bruggeman D. A. G., 1935, *Annalen der Physik*, 416, 636
- Bushouse H., et al., 2025, JWST Calibration Pipeline, Zenodo, doi:10.5281/zenodo.15178003
- Dominik C., Min M., Tazaki R., 2021, Astrophysics Source Code Library, p. ascl:2104.010
- Dorschner J., Begemann B., Henning T., Jaeger C., Mutschke H., 1995, *Astronomy and Astrophysics*, 300, 503
- Dullemond C. P., Monnier J. D., 2010, *Annual Review of Astronomy and Astrophysics*, 48, 205
- Espaillet C., Furlan E., D'Alessio P., Sargent B., Nagel E., Calvet N., Watson D. M., Muzerolle J., 2011, *The Astrophysical Journal*, 728, 49
- Espaillet C., et al., 2014, *Protostars and Planets VI*, pp 497–520
- Evans N. J., et al., 2003, *Publications of the Astronomical Society of the Pacific*, 115, 965
- Flock M., Fromang S., Turner N. J., Benisty M., 2017, *The Astrophysical Journal*, 835, 230
- Foreman-Mackey D., Hogg D. W., Lang D., Goodman J., 2013, *Publications of the Astronomical Society of the Pacific*, 125, 306
- Furlan E., et al., 2006, *The Astrophysical Journal Supplement Series*, 165, 568
- Furlan E., et al., 2009, *The Astrophysical Journal*, 703, 1964
- Gail H.-P., 2004, *Astronomy & Astrophysics*, 413, 571
- Gangi M., et al., 2022, *Astronomy and Astrophysics*, 667, A124
- Gardner J. P., et al., 2006, *Space Science Reviews*, 123, 485
- Giacalone S., Teitler S., Königl A., Krijt S., Ciesla F. J., 2019, *The Astrophysical Journal*, 882, 33
- Glauser A. M., Güdel M., Watson D. M., Henning T., Schegerer A. A., Wolf S., Audard M., Baldovin-Saavedra C., 2009, *Astronomy & Astrophysics*, 508, 247
- Goodman J., Weare J., 2010, *Communications in Applied Mathematics and Computational Science*, 5, 65
- Grankin K. N., Bouvier J., Herbst W., Melnikov S. Y., 2008, *Astronomy & Astrophysics*, 479, 827
- Guerra-Alvarado O. M., van der Marel N., Williams J. P., Pinilla P., Mulders G. D., Lambrechts M., Sanchez M., 2025, *Astronomy and Astrophysics*, 696, A232
- Hartmann L., Kenyon S. J., 1996, *Annual Review of Astronomy and Astrophysics*, 34, 207
- Honda M., Kataza H., Okamoto Y. K., Miyata T., Yamashita T., Sako S., Takubo S., Onaka T., 2003, *The Astrophysical Journal*, 585, L59
- Houck J. R., et al., 2004, *The Astrophysical Journal Supplement Series*, 154, 18
- IRS Instrument Team & Science User Support Team 2021, IRS Instrument Handbook, doi:10.26131/IRSA487
- Jaeger C., Molster F. J., Dorschner J., Henning Th., Mutschke H., Waters L. B. F. M., 1998, *Astronomy and Astrophysics*, 339, 904
- Jäger C., Dorschner J., Mutschke H., Posch Th., Henning Th., 2003, *Astronomy and Astrophysics*, 408, 193
- Jang H., Waters R., Kamp I., Dullemond C. P., 2024a, *Astronomy & Astrophysics*, 687, A275
- Jang H., et al., 2024b, *Astronomy and Astrophysics*, 691, A148
- Juhász A., et al., 2010, *The Astrophysical Journal*, 721, 431
- Kaeufer T., Min M., Woitke P., Kamp I., Arabhavi A. M., 2024, *Astronomy and Astrophysics*, 687, A209
- Kemper F., Vriend W. J., Tielens A. G. G. M., 2004, *The Astrophysical Journal*, 609, 826
- Kessler-Silacci J., et al., 2006, *The Astrophysical Journal*, 639, 275
- Kitamura R., Pilon L., Jonasz M., 2007, *Applied Optics*, 46, 8118
- Lebouteiller V., Barry D. J., Goes C., Sloan G. C., Spoon H. W. W., Weedman D. W., Bernard-Salas J., Houck J. R., 2015, *The Astrophysical Journal Supplement Series*, 218, 21
- Long F., et al., 2018, *The Astrophysical Journal*, 869, 17
- Mainzer A., et al., 2011, *The Astrophysical Journal*, 743, 156
- Min M., Hovenier J. W., de Koter A., 2003, *Astronomy & Astrophysics*, 404, 35
- Min M., Hovenier J. W., de Koter A., 2005, *Astronomy and Astrophysics*, 432, 909
- Min M., Waters L. B. F. M., de Koter A., Hovenier J. W., Keller L. P., Markwick-Kemper F., 2007, *Astronomy and Astrophysics*, 462, 667
- Min M., Rab C., Woitke P., Dominik C., Ménard F., 2016, *Astronomy and Astrophysics*, 585, A13
- Morales-Calderón M., et al., 2011, *The Astrophysical Journal*, 733, 50
- Olofsson J., et al., 2009, *Astronomy & Astrophysics*, 507, 327
- Olofsson J., Augereau J.-C., van Dishoeck E. F., Merín B., Grosso N., Ménard F., Blake G. A., Monin J.-L., 2010, *Astronomy & Astrophysics*, 520, A39
- Orcajo S., et al., 2025, *The Astrophysical Journal Letters*, Volume 984, Issue 2, id.L57, 13 pp., 984, L57
- Park W., et al., 2021, *The Astrophysical Journal*, 920, 132
- Rigby J., et al., 2023, *Publications of the Astronomical Society of the Pacific*, 135, 048001
- Shappee B. J., et al., 2014, *The Astrophysical Journal*, 788, 48
- Stauffer J., et al., 2014, *The Astronomical Journal*, 147, 83
- Suto H., et al., 2006, *Monthly Notices of the Royal Astronomical Society*, 370, 1599
- Tamanai A., Mutschke H., Blum J., Meeus G., 2006, *The Astrophysical Journal*, 648, L147
- Virtanen P., et al., 2020, *Nature Methods*, 17, 261
- Wang S., Chen X., 2019, *The Astrophysical Journal*, 877, 116
- Watson D. M., et al., 2008, *The Astrophysical Journal Supplement Series*, 180, 84
- Werner M. W., et al., 2004, *The Astrophysical Journal Supplement Series*, 154, 1
- Williams J. P., Cieza L. A., 2011, *Annual Review of Astronomy and Astrophysics*, 49, 67
- Woitke P., et al., 2016, *Astronomy & Astrophysics*, 586, A103
- Wright E. L., et al., 2010, *The Astronomical Journal*, 140, 1868
- Wu X., Roby T., Ly L., 2010, in *Observatory Operations: Strategies, Processes, and Systems III*. SPIE, pp 263–268, doi:10.1117/12.857728
- Xin Z., Espaillet C. C., Rilinger A. M., Ribas Á., Macías E., 2023, *The Astrophysical Journal*, 942, 4
- van Boekel R., Min M., Waters L. B. F. M., de Koter A., Dominik C., van den Ancker M. E., Bouwman J., 2005, *Astronomy & Astrophysics*, 437, 189

APPENDIX A: THE RESULTS USING THE SIMPLE AVERAGING METHOD FOR CRYSTALLINE SILICATES OPTICAL PROPERTIES

We performed the same analysis using the simple averaging method for crystalline silicates optical properties (see Section 3.2). The fitting results for Sz 96 and IP Tau are presented in Figs A1 and A2, respectively. The best-fit parameters are summarised in Table A1. The temperature and c parameters are shown in Figs A3 and A4, respectively.

For IP Tau, the trends in the variability of the parameters remain consistent with those obtained using the Bruggeman rule in Section 4. However, for Sz 96, the mid-plane temperature decreases by 33 K, whereas that of the crystalline dust component increases by 147 K, which are different compared to the variabilities presented in Section 4. Consequently, the c parameter for the mid-plane increases by 213%, while that for the crystalline dust decreases by 89%, both exhibiting variability trends different from those shown in Section 4.

Therefore, we note that the interpretation of the variability for IP Tau remains robust, whereas that for the mid-plane and crystalline surface dust in Sz 96 likely depends on the method used to calculate the optical properties of crystalline silicates.

APPENDIX B: THE POSTERIOR DISTRIBUTIONS

The posterior distributions of the temperature parameters are shown in Fig. B1 for Sz 96 and Fig. B2 for IP Tau. These distributions are

Table A1. The medians and the 0.025 and 0.975 quantiles of the posterior distributions of the parameters and the RMS residual for each spectrum. The parameter $c_{\text{sur}}^{\text{am}}$ and $c_{\text{sur}}^{\text{cr}}$ represent the sum over each type of dust component. The units of c parameters are 10^{-18} sr for the rim, 10^{-15} sr for the mid-plane, and 10^{-20} g cm^{-2} sr for the surface components.

Target	Data	T_{rim} (K)	T_{mid} (K)	$T_{\text{sur}}^{\text{am}}$ (K)	$T_{\text{sur}}^{\text{cr}}$ (K)	c_{rim}	c_{mid}	$c_{\text{sur}}^{\text{am}}$	$c_{\text{sur}}^{\text{cr}}$	Residual (RMS)
Sz 96	SST	984^{+17}_{-16}	163^{+3}_{-2}	440^{+15}_{-14}	213^{+11}_{-11}	$5.4^{+0.2}_{-0.2}$	$1.5^{+0.1}_{-0.1}$	$3.7^{+0.5}_{-0.4}$	12^{+3}_{-2}	2.1%
	JWST	$1079^{+0.4}_{-0.4}$	$130^{+0.1}_{-0.1}$	$415^{+0.3}_{-0.3}$	$360^{+1.0}_{-0.9}$	$3.7^{+0.01}_{-0.01}$	$4.7^{+0.01}_{-0.01}$	$6.0^{+0.02}_{-0.02}$	$1.3^{+0.01}_{-0.01}$	2.5%
IP Tau	SST	1304^{+96}_{-85}	154^{+3}_{-4}	463^{+51}_{-38}	1031^{+449}_{-584}	$3.1^{+0.5}_{-0.4}$	$3.3^{+0.3}_{-0.2}$	$3.0^{+1.3}_{-0.9}$	$0.02^{+0.24}_{-0.01}$	3.4%
	JWST	$1224^{+0.5}_{-0.6}$	$154^{+0.1}_{-0.1}$	$442^{+0.3}_{-0.3}$	$188^{+0.5}_{-0.6}$	$4.2^{+0.01}_{-0.01}$	$3.5^{+0.01}_{-0.01}$	$4.9^{+0.01}_{-0.01}$	$4.2^{+0.06}_{-0.06}$	1.6%

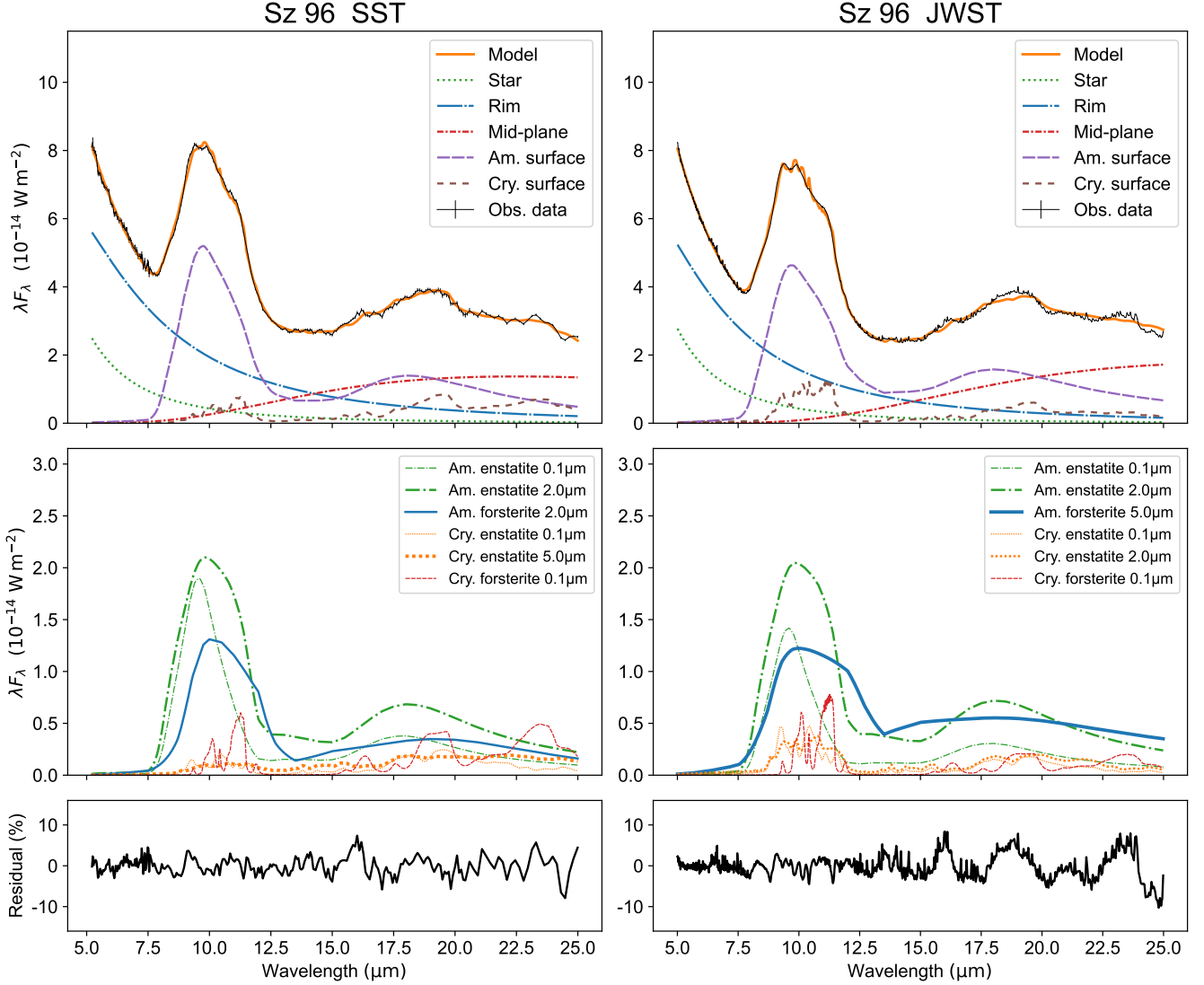


Figure A1. Fitting results of Sz 96 using the simple averaging method for crystalline silicates optical properties: overall fitting results (top), contributions from each dust component (middle), and residual of the best-fitting model (bottom) for SST (left) and JWST (right). In the middle panel, the emissions from the star, rim, and mid-plane, as well as components contributing less than 0.5% to the total flux, are not shown.

those obtained using the Bruggeman method. Most parameters exhibit clear peaks, except for $T_{\text{sur}}^{\text{cr}}$ in the SST data of IP Tau, whose posterior distribution spans from a lower limit of approximately 300 K to an upper limit corresponding to the dust sublimation temperature of about 1500 K. Within this range $T_{\text{sur}}^{\text{cr}}$ significantly affects only $c_{\text{sur}}^{\text{cr}}$.

In the best-fitting model shown in the left panel of Fig. 4, we set $T_{\text{sur}}^{\text{cr}}$ equal to be the best-fitting value of T_{rim} .

This paper has been typeset from a \LaTeX file prepared by the author.

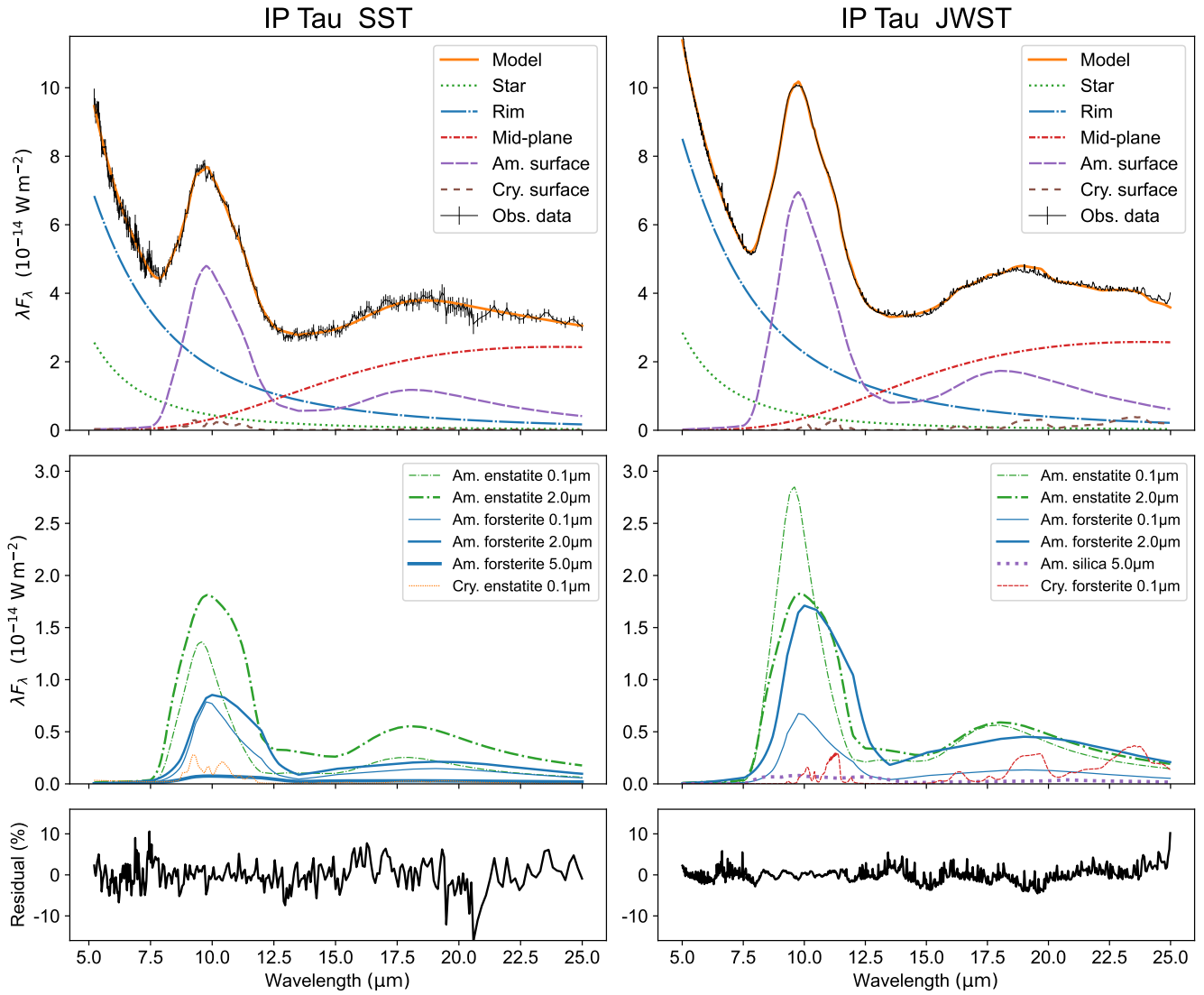


Figure A2. Fitting results of IP Tau using the simple averaging method for crystalline silicates optical properties: overall fitting results (top), contributions from each dust component (middle), and residual of the best-fitting model (bottom) for SST (left) and JWST (right). In the middle panel, the emissions from the star, rim, and mid-plane, as well as components contributing less than 0.5% to the total flux, are not shown.

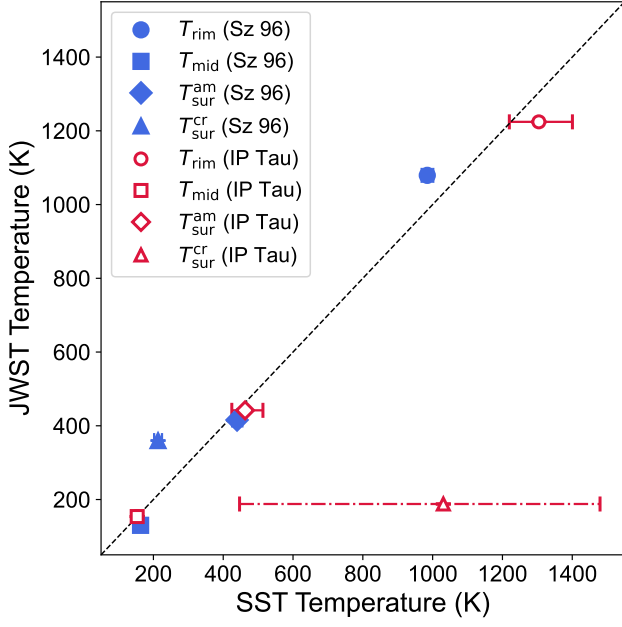


Figure A3. The temperature parameters for Sz 96 (filled symbols) and IP Tau (open symbols) using the simple averaging method for crystalline silicates optical properties. The x-axis represents SST temperatures, while the y-axis represents JWST temperatures. The error bars represent the 0.025 and 0.975 quantiles of the posterior distributions of the parameters. The dashed line shows where the SST and JWST temperatures would be equal. $T_{\text{sur}}^{\text{cr}}$ for the SST data of IP Tau is unconstrained.

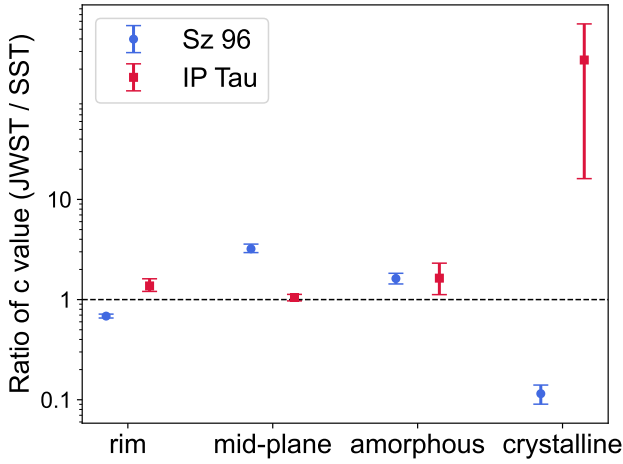


Figure A4. The ratio of the c value (JWST/SST) for Sz 96 (circles) and IP Tau (squares) using the simple averaging method for crystalline silicates optical properties. The error bars represent the 0.025 and 0.975 quantiles of the ratio, computed using samples drawn from the posterior distributions of the c values for the JWST and SST data. The c value for each component represents the solid angle as seen by the observer for the rim and mid-plane, and the dust mass in the surface region for amorphous and crystalline components.

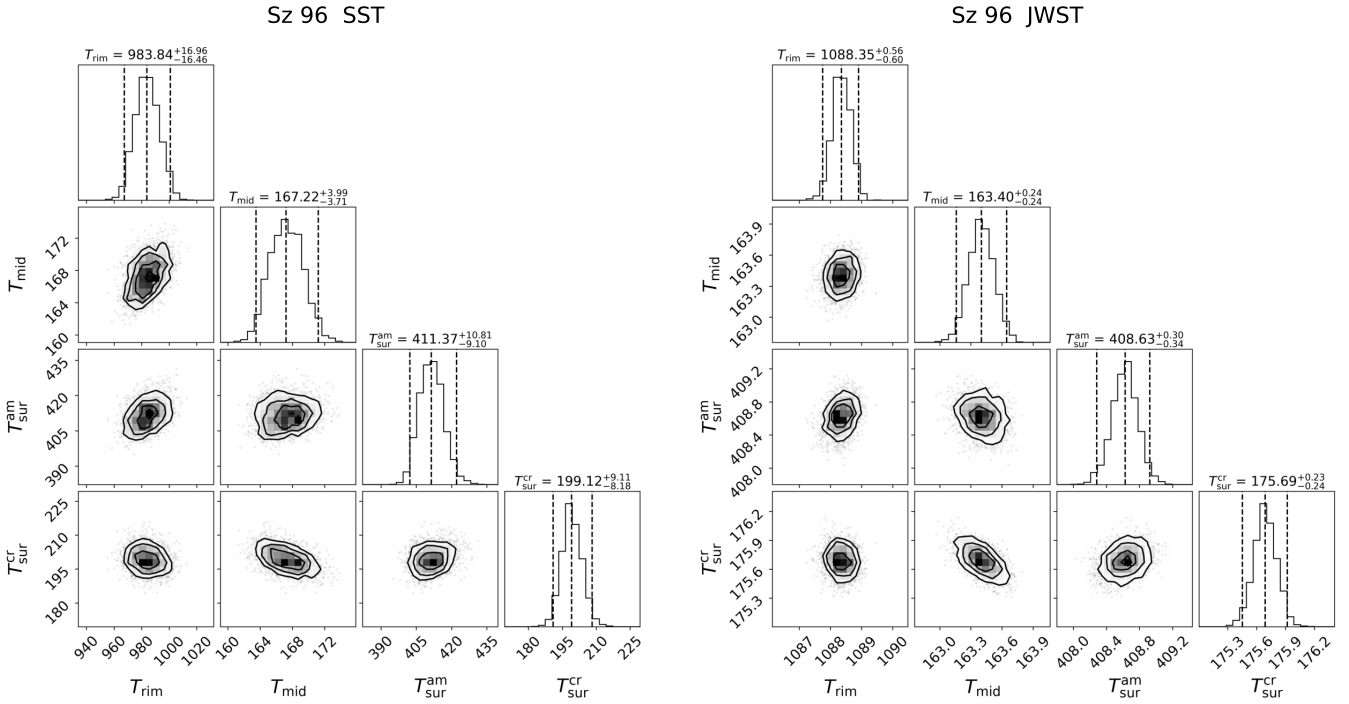


Figure B1. The posterior distributions of the temperature parameters for the SST (left) and JWST (right) data of Sz 96. The dashed lines correspond to the quantiles $q = 0.025, 0.5, 0.975$.

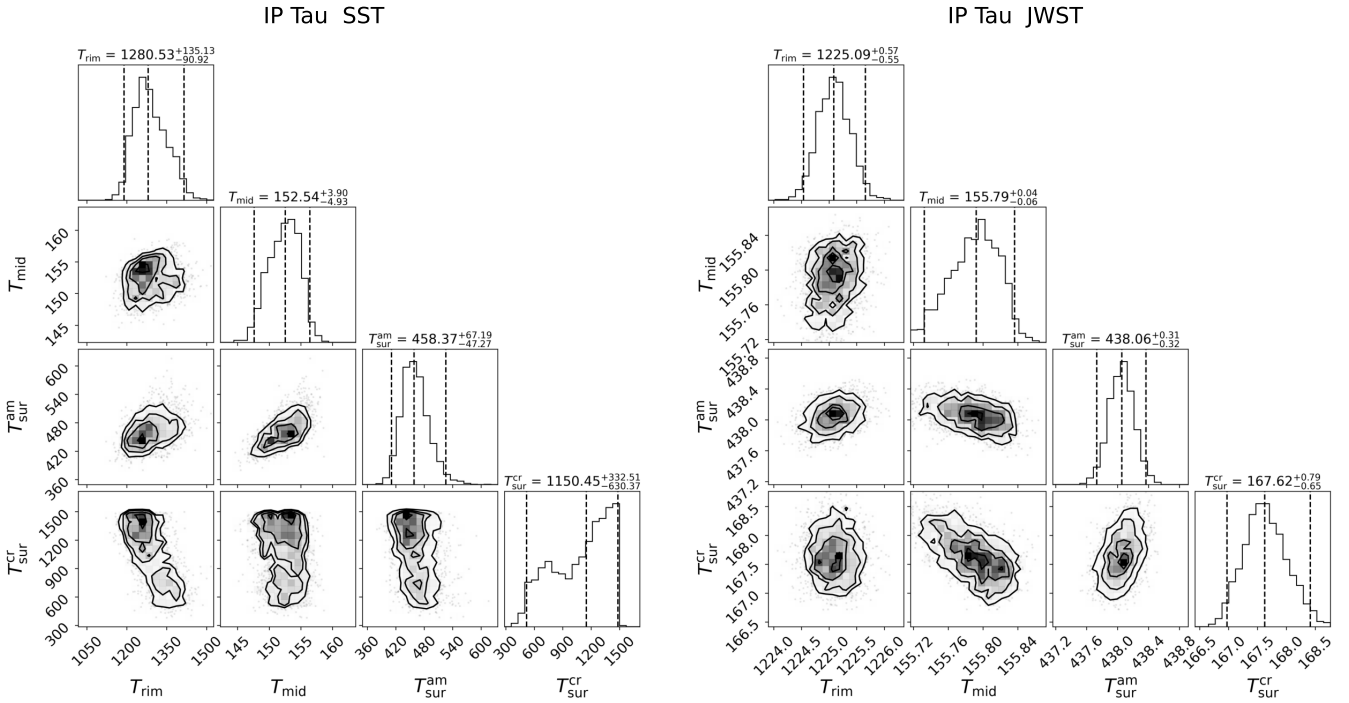


Figure B2. The posterior distributions of the temperature parameters for the SST (left) and JWST (right) data of IP Tau. The dashed lines correspond to the quantiles $q = 0.025, 0.5, 0.975$. For the SST data of IP Tau, the posterior distribution of $T_{\text{sur}}^{\text{cr}}$ is broad and extends to the upper limit of the prior range, indicating that this parameter is unconstrained. This is the only case among all parameters and datasets where the posterior distribution reaches the prior boundary.